

# Match4Annotate: Propagating Sparse Video Annotations via Implicit Neural Feature Matching

Zhuorui Zhang<sup>1\*</sup>, Roger Pallarès-López<sup>1\*</sup>, Praneeth Namburi<sup>2,3</sup>, and Brian W. Anthony<sup>1,2,3</sup>

<sup>1</sup> Department of Mechanical Engineering, Massachusetts Institute of Technology, Cambridge, USA

<sup>2</sup> Institute for Medical Engineering and Science, Massachusetts Institute of Technology, Cambridge, USA

<sup>3</sup> MIT.nano Immersion Lab, Massachusetts Institute of Technology, Cambridge, USA  
`banthony@mit.edu`

**Abstract.** Acquiring per-frame video annotations remains a primary bottleneck for deploying computer vision in specialized domains such as medical imaging, where expert labeling is slow and costly. Label propagation offers a natural solution, yet existing approaches face fundamental limitations. Video trackers and segmentation models can propagate labels within a single sequence but require per-video initialization and cannot generalize across videos. Classic correspondence pipelines operate on detector-chosen keypoints and struggle in low-texture scenes, while dense feature matching and one-shot segmentation methods enable cross-video propagation but lack spatiotemporal smoothness and unified support for both point and mask annotations. We present Match4Annotate, a lightweight framework for both intra-video and inter-video propagation of point and mask annotations. Our method fits a SIREN-based implicit neural representation to DINOv3 features at test time, producing a continuous, high-resolution spatiotemporal feature field, and learns a smooth implicit deformation field between frame pairs to guide correspondence matching. We evaluate on three challenging clinical ultrasound datasets. Match4Annotate achieves state-of-the-art inter-video propagation, outperforming feature matching and one-shot segmentation baselines, while remaining competitive with specialized trackers for intra-video propagation. Our results show that lightweight, test-time-optimized feature matching pipelines have the potential to offer an efficient and accessible solution for scalable annotation workflows.

**Keywords:** Video annotation · Feature matching · Implicit neural representations · Medical imaging · Cross-video propagation

---

\* Equal contribution.

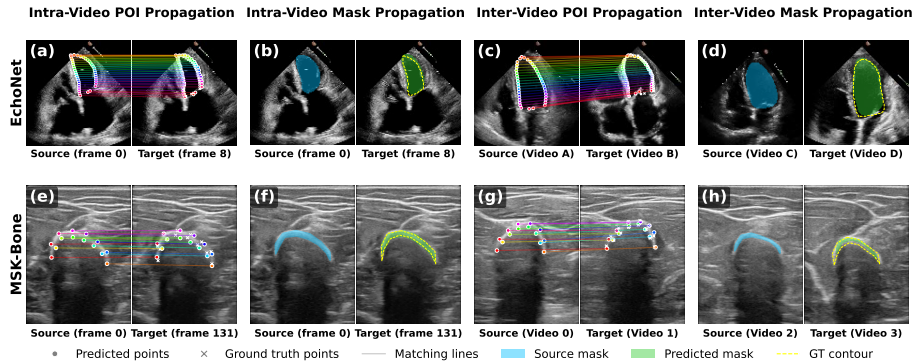


**Fig. 1: Overview of Match4Annotate.** Annotation propagation across two medical ultrasound datasets. Each panel shows a source frame (left) with ground-truth annotations and a target frame (right) with propagated predictions. (a–b) Intra-video propagation on EchoNet cardiac ultrasound: (a) boundary point tracking with colored matching lines connecting corresponding source and predicted points, and (b) segmentation mask propagation. (c–d) Inter-video propagation on EchoNet between different subject videos. (e–f) Intra-video propagation on MSK-Bone musculoskeletal ultrasound. (g–h) Inter-video propagation on MSK-Bone across different subject videos.

## 1 Introduction

Acquiring dense per-frame annotations (*e.g.*, pixel-level masks or tracked points) remains a primary bottleneck for deploying computer vision systems in specialized domains. In medical imaging, expert annotation time is costly (often \$200–500/hour [35]), making large-scale temporal labeling prohibitively expensive. For example, annotating EchoNet-Dynamic [23] (10,030 cardiac ultrasound videos) at standard clinical temporal density (32 frames/video), would require approximately 1,900 hours of expert time, a scale that most institutions cannot afford.

A natural strategy to reduce annotation effort is label propagation: given a small number of user annotations, automatically transfer them to additional frames. State-of-the-art zero-shot trackers and video object segmentation models have made propagation practical within a single video [2, 14, 26, 41]. However, these approaches are fundamentally designed around temporal continuity and typically require per-video initialization (points, masks, or memory prompts). Models such as SAM2 [26], CoTracker3 [13], and XMem [6] can propagate labels within a sequence, but cannot generalize those labels across different videos.

Classic correspondence pipelines and learned local features (*e.g.*, SuperPoint [7], DISK [34], LightGlue [18], XFeat [25]) alleviate this problem by providing strong automatic matching, but they typically operate on detector-chosen keypoints, making it impractical to propagate user-specified points or dense masks at arbitrary locations in low-texture, low-contrast scenes where local appearance provides weak cues. To address these limitations, recent foundation-model corre-

spondence methods [11, 32, 40] leverage semantic representations to enable user-queryable point transfer even across unrelated images, strengthening cross-video matching baselines. However, converting pairwise correspondences into a reliable annotation propagation tool remains challenging: it should handle both points and masks, enforce spatiotemporal smoothness to prevent drift and jitter, and remain robust to domain shift, even when the underlying features come from models pretrained primarily on natural images.

**Our Approach.** We introduce MATCH4ANNOTATE, a lightweight framework for annotation propagation that supports both *intra-video* (within a video) and *inter-video* (across videos) transfer of pixel-level labels. Our method leverages learned, high-resolution implicit neural feature representations to propagate point and mask annotations across space and time. We evaluate on three challenging clinical ultrasound datasets, including echocardiography and musculoskeletal imaging. Our approach is built around three key components:

(1) *High-resolution smooth spatiotemporal semantic features via implicit neural representations:* We adopt a test-time optimization strategy that learns continuous spatiotemporal mappings  $((x, y, t) \mapsto f_\theta(x, y, t) \in \mathbb{R}^d)$  from coordinates to high-resolution feature vectors. Building upon FeatUp [12], we fit DINOv3 [28] features with a SIREN [29] network using sinusoidal activations, enabling feature queries at arbitrary spatial resolutions while promoting smooth variation over space and time.

(2) *Flow-guided matching correspondence:* We learn an *implicit deformation field* with a separate SIREN  $g_\phi : \mathbb{R}^2 \rightarrow \mathbb{R}^2$  that predicts per-coordinate displacements  $(\Delta x, \Delta y) = g_\phi(x, y)$  for a pair of source and target frames. We use this learned deformation as a prior to guide matching, improving correspondence reliability for propagating user annotations.

(3) *Efficient test-time training:* Our lightweight architecture trains on individual videos in minutes on consumer hardware (RTX 4090). The automatic optimization requires no user interaction beyond providing the initial source annotation.

Together, these components make Match4Annotate a scalable and adaptable solution for annotation propagation in specialized video domains (Figure 1).

### Summary of Contributions.

- We propose Match4Annotate, a framework for annotation propagation that supports both intra-video and inter-video transfer of point and mask labels.
- We introduce a high-resolution, smooth spatiotemporal feature field using test-time SIREN optimization to upsample DINOv3 features on videos.
- We develop a flow-guided matching strategy that improves correspondence reliability.
- We validate design choices through ablations and demonstrate state-of-the-art inter-video propagation, outperforming feature matching and few-shot segmentation baselines.

## 2 Related Work

**Implicit Neural Representations.** Coordinate-based neural networks map input coordinates to signal values, enabling continuous signal representation [31, 38]. SIREN [29] introduced sinusoidal activations to capture high-frequency content with smooth derivatives. While NeRF [20] and instant-NGP [21] focus on 3D scene reconstruction, we extend implicit representations to spatiotemporal video features for annotation propagation.

**Feature Upsampling and Foundation Models.** Vision foundation models such as DINO [4] and DINOv2 [22] provide strong semantic features but at a low resolution [10]. FeatUp [12] addresses this by training coordinate-based MLPs to upsample features from spatial coordinates  $(x, y)$ . DINOv3 [28] improves the quality of dense features and introduces strategies to better support higher-resolution applications, yet it does not explicitly enforce spatiotemporal smoothness across frames. Motivated by this gap, we extend implicit feature upsampling to the spatiotemporal domain  $(x, y, t)$  using SIREN architectures, enabling smooth, high-resolution feature fields for video annotation propagation.

**Video Point and Mask Tracking.** Dense video correspondence is fundamental to annotation propagation. Optical flow methods [33, 39] excel at short-range motion but are limited to consecutive frames. Point tracking methods extend correspondence over longer spans: TAPNext [41] uses masked-token decoding, CoTracker3 [13, 14] tracks multiple points jointly, and Track-On2 [1, 2] introduces online tracking with external memory. Video object segmentation methods like XMem [6], STCN [5] and SAM 2 [26] achieve temporal consistency through memory mechanisms. While effective within individual videos, these methods require manual per-video initialization and cannot transfer annotations across videos. Our implicit neural representation learns smooth feature fields from foundation model supervision, enabling correspondence that generalizes across both time and different video instances without manual intervention.

**Correspondence Matching Methods and Few-Shot Segmentation.** Few-shot segmentation methods [3, 37] segment query images given support examples. UniverSeg [3] demonstrates few-shot medical segmentation with support images. Matcher [19] achieves reference-based SAM [16, 17] segmentation from one example. However, these methods produce segmentation masks rather than point-level correspondences and do not leverage temporal consistency. In parallel, correspondence methods based on foundation representations, including RoMa [11], diffusion-based features [27] such as DIFT [32], and unified matching models such as MATCHA [40], enable user-queryable matches between image pairs, offering a strong baseline for cross-video point transfer. However, these models are pretrained on natural images and can degrade under domain shift in specialized domains. Our method targets these propagation requirements by refining pretrained features at test time into a smooth spatiotemporal field and using flow-guided regularization, improving the stability of point and mask transfer within and across videos under domain shift.

**Test-Time Adaptation.** Test-time training adapts models to individual instances [30, 36]. Our approach optimizes implicit neural representations from

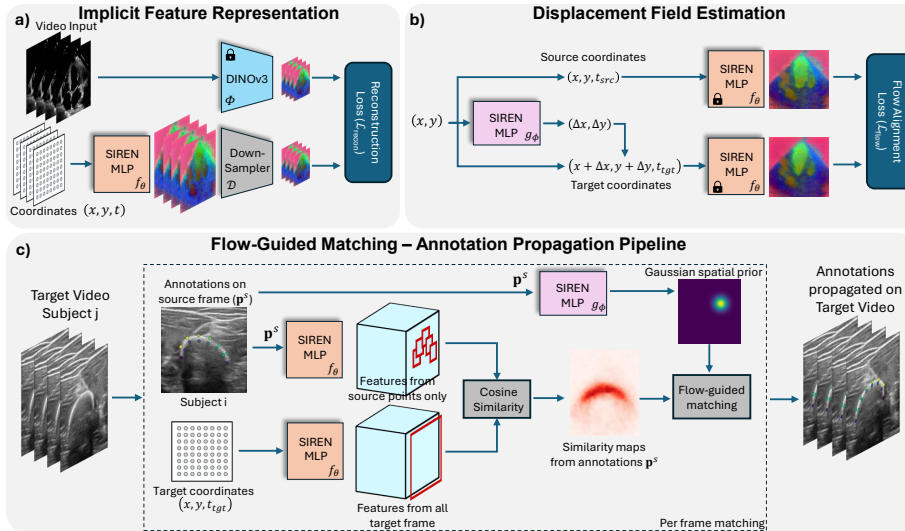


**Fig. 2: Match4Annotate workflow.** a) Given a video, we fit an implicit SIREN to represent DINOv3 features as a continuous, high-resolution spatiotemporal field  $f_\theta(x, y, t)$ , enabling feature queries at arbitrary coordinates. b) For a source–target pair (across frames or videos), we optimize a second SIREN  $g_\phi$  to predict per-coordinate 2D displacements, yielding a smooth deformation prior via feature-alignment and regularization. c) We propagate user annotations by combining this flow-guided prior with feature matching: features from  $f_\theta$  are compared (cosine similarity) to select correspondences, improving stability over naive pairwise matching.

scratch per video, fitting foundation-model features. This allows specialization to each sequence while preserving semantic consistency inherited from foundation model features.

### 3 Method

#### 3.1 Overview

Given a video  $\mathcal{V} = \{I_1, I_2, \dots, I_T\}$  and annotations on a source frame—either individual points of interest (POI) or a binary segmentation mask—our goal is to propagate these annotations to target frames within the same video (*intra-video*) or across different videos of the same anatomy (*inter-video*).

Our method has two core components. First, we learn a continuous spatiotemporal feature field  $f_\theta$  by fitting a SIREN [29] implicit neural representation to frozen vision foundation model (VFM) features (Fig. 2a), enabling feature queries at arbitrary spatial resolution (Sec. 3.3). Second, we establish dense correspondences via a flow-guided matching strategy that trains a lightweight displacement SIREN  $g_\phi$  to predict spatial deformations between frames (Fig. 2b), combining learned flow priors with feature-based refinement (Sec. 3.4).

We address two complementary tasks:

- **Point propagation.** Individual landmark points are matched from source to target via the flow-guided correspondence field. For intra-video propagation, we evaluate with  $\delta_{\text{avg}}$  (TAP-Vid protocol [8]). For inter-video propagation, we report PCK at multiple thresholds (Sec. 3.6).
- **Mask propagation.** Binary segmentation masks are propagated via an interior point method. We extract a dense set of interior points from the source mask, propagate them to the target frame via flow-guided matching, and reconstruct a target mask via kernel density estimation (KDE) followed by thresholding, evaluated by Dice coefficient (Secs. 3.5 and 3.6).

### 3.2 Feature Extraction

We extract dense features from each frame  $I_t$  using DINOv3-ViT-S/16 [28] as our frozen VFM  $\Phi$ , producing a spatial grid of patch tokens:

$$F_t = \Phi(I_t) \in \mathbb{R}^{H' \times W' \times D} \quad (1)$$

where  $H' = W' = S/p$  is the spatial grid resolution determined by the input size  $S$  and patch size  $p$ , and  $D$  is the feature dimension. All features are  $\ell_2$ -normalized. The VFM is used only for feature extraction and is not fine-tuned.

### 3.3 Spatiotemporal Implicit Feature Representation

**Problem Formulation.** Given video features  $\mathcal{F} = \{F_1, \dots, F_T\}$  extracted by  $\Phi$ , our goal is to learn a continuous function  $f_\theta : \mathbb{R}^3 \rightarrow \mathbb{R}^D$  that maps any spatiotemporal coordinate  $(x, y, t)$  to a  $D$ -dimensional feature vector:

$$f_\theta(x, y, t) \in \mathbb{R}^D, \quad (x, y, t) \in [1, W] \times [1, H] \times [1, T] \quad (2)$$

This implicit representation enables querying features at arbitrary resolutions, facilitating dense correspondence establishment at sub-patch granularity.

**Network Architecture.** We adopt SIREN [29] with periodic activation functions  $\phi(x) = \sin(\omega x)$ . We choose SIREN over alternative implicit representations for three reasons: (1) sinusoidal activations enable continuous coordinate-based signal representations with controllable frequency content, which helps mitigate interpolation artifacts when querying features at arbitrary spatial resolutions; (2) the periodic activations yield well-behaved higher-order derivatives, enabling stable gradient-based flow estimation; and (3) the periodic structure provides an inductive bias for modeling cyclic anatomical motion in ultrasound videos. We provide justification of this design choice over other common candidates in the Supplementary Materials.

Our network consists of  $L$  fully-connected layers with  $H_{\text{dim}}$  hidden dimensions (additional details in the Supplementary Materials). Different from [12], we use coordinates only  $(x, y, t)$  without intensity  $I_t(x, y)$  to avoid spurious correlations from ultrasound speckle noise. This prioritizes semantic consistency over texture fidelity.

**Training Objective.** We train  $f_\theta$  to reproduce the VFM features at high resolution via a learned downsampling operator. Specifically,  $f_\theta$  is evaluated on a dense high-resolution grid  $\Omega_{\text{HR}}$  of size  $H \times W$ , then a convolution-based downsampler  $\mathcal{D}$  maps the output back to the VFM resolution:

$$\mathcal{L}_{\text{recon}} = \frac{1}{N} \sum_{i=1}^N \|\mathcal{D}(f_\theta(x_i, y_i, t_i)) - F_{t_i}(x_i, y_i)\|_2^2 \quad (3)$$

where  $\mathcal{D} : \mathbb{R}^{H \times W \times D} \rightarrow \mathbb{R}^{H' \times W' \times D}$  is a learnable depthwise convolution with non-negative, normalized weights ensuring the downsampled features remain in a valid range (see the Supplementary Material for details). We optimize using Adam [15]. After training,  $f_\theta$  can be queried at any continuous coordinate  $(x, y, t)$ .

### 3.4 Flow-Guided Correspondence

Given source annotations  $\{\mathbf{p}_i^s\}_{i=1}^K$  on source frame  $t_{\text{src}}$ , we propagate each point to a target frame  $t_{\text{tgt}}$  using a learned flow prior combined with feature-based refinement, querying the continuous feature field  $f_\theta$  directly.

**Displacement Field Estimation.** We estimate a dense deformation field using a lightweight displacement SIREN  $g_\phi : \mathbb{R}^2 \rightarrow \mathbb{R}^2$  that predicts per-pixel spatial displacements from source to target. For a given source-target frame pair, the network maps each spatial location to a displacement vector:

$$(\Delta x, \Delta y) = g_\phi(x, y) \quad (4)$$

Since  $f_\theta$  is a continuous function, we can directly query it at displaced coordinates. The displacement SIREN is optimized to align features across all valid spatial positions:

$$\mathcal{L}_{\text{flow}} = \frac{1}{M} \sum_{i=1}^M \|f_\theta(x_i + \Delta x_i, y_i + \Delta y_i, t_{\text{tgt}}) - f_\theta(x_i, y_i, t_{\text{src}})\|_2^2 + \lambda_1 \cdot \mathcal{L}_{\text{TV}} + \lambda_2 \cdot \mathcal{L}_{\text{L1}} \quad (5)$$

where  $\mathcal{L}_{\text{TV}}$  is total variation regularization encouraging spatial smoothness of the displacement field, and  $\mathcal{L}_{\text{L1}} = \frac{1}{M} \sum_i \|g_\phi(x_i, y_i)\|_1$  penalizes overall displacement magnitudes, acting as a prior avoiding unnecessary deformation on flat regions.

**Flow-Guided Matching.** The predicted displacement provides a data-driven spatial prior. We use the flow-predicted position as the center of a Gaussian weighting kernel combined with feature cosine similarity:

$$\hat{\mathbf{p}} = \mathbf{p}^s + g_\phi(\mathbf{p}^s) \quad (6)$$

$$\mathbf{p}^* = \arg \max_{\mathbf{p} \in \Omega} \cos(f_\theta(\mathbf{p}^s, t_s), f_\theta(\mathbf{p}, t)) \cdot \exp\left(-\frac{\|\mathbf{p} - \hat{\mathbf{p}}\|^2}{2\sigma^2}\right) \quad (7)$$

where  $\cos(\mathbf{a}, \mathbf{b}) = \mathbf{a}^\top \mathbf{b} / (\|\mathbf{a}\| \|\mathbf{b}\|)$  denotes cosine similarity,  $\Omega$  is a dense spatial sampling of the target frame, and  $\sigma$  adapts to the annotation canvas size. This formulation combines the large-displacement capability of the learned flow field with the discriminative power of feature-based refinement under a spatial prior, resolving local ambiguities in regions with repetitive structure.

### 3.5 Mask Propagation via Interior Point Method

For segmentation tasks, rather than propagating only contour boundary points and reconstructing the mask from potentially noisy boundary predictions, we employ an interior point method that densely samples the annotated region.

**Interior Point Generation.** Given a source binary mask  $M_{\text{src}}$ , we extract a dense set of interior points using the Euclidean distance transform:

$$\mathcal{I}_{\text{src}} = \{(x, y) \mid \text{EDT}(x, y; M_{\text{src}}) \geq d_{\text{min}}\} \quad (8)$$

where  $\text{EDT}(x, y; M_{\text{src}})$  is the Euclidean distance from  $(x, y)$  to the nearest background pixel, and  $d_{\text{min}}$  controls the minimum distance from the mask boundary. This yields a set of interior pixel coordinates that densely cover the annotated region while excluding ambiguous boundary pixels.

**Point Propagation.** All interior points are propagated to the target frame using the flow-guided matching strategy (Sec. 3.4). Each point  $\mathbf{p} \in \mathcal{I}_{\text{src}}$  is mapped to its corresponding location  $\mathbf{p}^*$  in the target frame, producing a propagated interior point set  $\mathcal{I}_{\text{tgt}}$ .

**Mask Reconstruction via Kernel Density Estimation (KDE).** The propagated interior points are converted to a binary segmentation mask via kernel density estimation. We place unit impulses at each propagated point and convolve with a Gaussian kernel:

$$P(x, y) = \frac{1}{Z} \sum_{\mathbf{p}_k^* \in \mathcal{I}_{\text{tgt}}} \exp\left(-\frac{(x - x_k^*)^2 + (y - y_k^*)^2}{2\sigma_{\text{KDE}}^2}\right) \quad (9)$$

where  $Z$  normalizes  $P$  to  $[0, 1]$ . The binary mask is obtained by thresholding:

$$M_{\text{pred}}(x, y) = \mathbf{1}[P(x, y) \geq \tau] \quad (10)$$

The KDE parameters ( $\sigma_{\text{KDE}}, \tau$ ) are tuned via grid search. This approach is more robust than direct polygon reconstruction from boundary vertices, as the dense interior sampling provides redundancy, i.e., individual point errors are smoothed out by the kernel, and the mask degrades gracefully rather than catastrophically when a subset of points are mismatched. We provide more details in the Supplementary Materials.

### 3.6 Evaluation Metrics

We evaluate point propagation and mask propagation with complementary metrics. Following the TAP-Vid protocol [9], we report  $\delta_{\text{avg}}$ , accuracy averaged over distance thresholds, on intra-video propagation tasks, with coordinates normalized to a  $256 \times 256$  canvas for scale invariance. For cross-video propagation, we report the Percentage of Correct Keypoints (PCK) at different distance thresholds, also normalized to the  $256 \times 256$  canvas. For segmentation evaluation, we used Dice coefficient between the predicted masks obtained from thresholding the probability map generated from the kernel density method (Sec. 3.5) and the ground-truth binary mask.

## 4 Experiments

We evaluate Match4Annotate on medical ultrasound video datasets, focusing on inter-video propagation as our primary contribution while validating intra-video performance against strong baselines.

### 4.1 Experimental Setup

**Datasets.** We evaluate our method on the publicly available EchoNet-Dynamic dataset [23] and two musculoskeletal ultrasound video datasets.

**EchoNet-Dynamic** comprises echocardiogram videos with expert annotations of the left ventricle endocardial border at both end-systole and end-diastole. These annotations are provided as point-based labels, which we leverage for our propagation experiments. To ensure consistent anatomical correspondence across videos, the annotated points follow a standardized ordering: starting at the long axis of the left ventricle and proceeding from the apex toward the mitral valve.

We additionally evaluate on two musculoskeletal (MSK) ultrasound video datasets of the upper arm, capturing tissue motion of the brachialis and triceps as well as the humerus. The first dataset, **MSK-POI** [24], is part of a broader multimodal arm-reaching dataset and contains one video per subject for 36 subjects. Each frame is annotated with 11 sparse points: 2 on the humerus, 4 within each muscle, and 1 at the muscle interface. Each trial comprises approximately 20 reaching cycles. The second dataset, **MSK-Bone**, contains 20 videos (one per subject) with manual segmentation masks of the humeral head. We convert each mask into 14 consistently ordered boundary points per frame to enable point-based propagation evaluation. This dataset was collected under IRB approval, and all annotations were produced by expert annotators.

**Evaluation Protocol.** For inter-video evaluation, we sample 200 EchoNet-Dynamic and 380 MSK-Bone source–target pairs, always pairing videos from different subjects. We exclude MSK-POI from inter-video evaluation because it provides only within-video (temporal) correspondences and lacks consistent

**Table 1: Inter-video annotation propagation** on EchoNet and MSK-Bone. We compare against few-shot segmentation methods (mask only, no point correspondence), 1-shot segmentation methods (mask only), and dense feature matching methods (point correspondence only, no mask). Multi-shot results (gray) use multiple support images and are not directly comparable. Best 1-shot result in **bold**, second underlined.

Method	EchoNet (200 pairs)		MSK-Bone (380 pairs)	
	PCK <sub>@.016/.031/.063</sub> ↑	Dice ↑	PCK <sub>@.016/.031/.063</sub> ↑	Dice ↑
<i>Few-Shot Segmentation</i>				
UniverSeg [3] (1-shot)	–	47.1±16.2	–	25.0±11.0
UniverSeg (2-shot)*	–	68.0±14.4	–	42.2±16.4
UniverSeg (3-shot)*	–	73.0±14.0	–	53.2±14.9
UniverSeg (5-shot)*	–	76.3±12.5	–	63.7±12.9
UniverSeg (10-shot)*	–	78.7±12.2	–	73.4±8.9
<i>1-Shot Segmentation</i>				
Matcher [19] (SemSAM)	–	<u>53.8±21.7</u>	–	<u>62.2±23.2</u>
Matcher [19] (SAM)	–	43.2±16.8	–	26.0±29.4
<i>Dense Feature Matching</i>				
RoMa [11] (indoor)	5.2 / 15.8 / 39.2	–	8.1 / 20.0 / 37.9	–
RoMa [11] (outdoor)	5.5 / 17.1 / <u>41.1</u>	–	6.9 / 17.8 / 34.5	–
DIFT [32]	4.0 / 11.7 / 27.2	–	<b>16.3</b> / <u>36.6</u> / 62.4	–
MATCHA [40]	<u>5.7</u> / <u>17.8</u> / 40.8	–	13.5 / 36.4 / <u>66.7</u>	–
Match4Annotate (Ours)	<b>6.1</b> / <b>18.4</b> / <b>46.7</b>	<b>76.3±12.3</b>	<u>15.5</u> / <b>40.0</b> / <b>74.3</b>	<b>69.0±11.9</b>

\*Uses multiple support images; not directly comparable to 1-shot methods.

semantic correspondence across subjects. For intra-video evaluation, we propagate annotations from a single labeled frame to all other frames within the same video; we evaluate on 100 EchoNet-Dynamic videos and on one randomly sampled reaching cycle per subject in MSK-POI. We report the metrics defined in Sec. 3.6: PCK at thresholds  $\{4, 8, 16\}$  pixels on a  $256 \times 256$  canvas for inter-video point propagation (i.e., PCK<sub>@.016/.031/.063</sub>),  $\delta_{\text{avg}}$  for intra-video point propagation, and Dice for mask propagation.

**Baselines.** For inter-video propagation, we compare against three categories: (1) *Few-shot segmentation*: UniverSeg [3] at 1-shot and multi-shot settings (2/3/5/10-shot, shown in gray as not directly comparable to 1-shot methods); (2) *1-shot segmentation*: Matcher [19] with SemSAM [17] and SAM [16] backbones; (3) *Dense feature matching*: RoMa [11] (indoor and outdoor pretrained models), DIFT [32], and MATCHA [40]. Segmentation methods provide masks only (no point correspondence), while dense matching methods provide point correspondences only (no masks). Match4Annotate uniquely provides both.

For intra-video propagation, we compare against: (1) *Video point trackers*: CoTracker3 [13], TAPNext [41], and TrackOn2 [2]; (2) *Video segmentation*: SAM 2 [26].

**Table 2: Intra-video annotation propagation** on EchoNet, MSK-POI, and MSK-Bone. We compare against video point trackers ( $\delta_{\text{avg}}$  only, no mask) and video segmentation (Dice only, no point correspondence). Best in **bold**, second underlined.

Method	EchoNet (100 videos)		MSK-POI (36 videos)	MSK-Bone (20 videos)	
	$\delta_{\text{avg}} \uparrow$	Dice $\uparrow$	$\delta_{\text{avg}} \uparrow$	$\delta_{\text{avg}} \uparrow$	Dice $\uparrow$
<i>Video POI Trackers</i>					
CoTracker3 [13]	<b>41.8±10.6</b>	–	<b>54.7±7.4</b>	<b>40.9±7.4</b>	–
TAPNext [41]	<u>41.6±11.3</u>	–	27.3±7.5	29.8±12.2	–
TrackOn2 [2]	34.9±9.6	–	<u>47.0±8.3</u>	32.4±9.4	–
<i>Video Segmentation</i>					
SAM 2 [26]	–	<b>86.7±5.5</b>	–	–	<b>86.3±2.3</b>
Match4Annotate (Ours)	31.7±11.5	<u>85.1±6.5</u>	41.8±8.8	<u>38.2±7.0</u>	<u>74.2±5.7</u>

## 4.2 Inter-Video Annotation Propagation

Tab. 1 reports our main cross-video propagation results for point correspondence and mask transfer. Qualitative comparisons are shown in Figs. 3 and 4, with additional examples provided in the Supplementary Material.

**Point correspondence.** On EchoNet, Match4Annotate achieves the highest PCK across all thresholds, outperforming RoMa and MATCHA, the next-best dense matching methods, by a clear margin, particularly at coarser thresholds. On MSK-Bone, Match4Annotate leads at the two coarser thresholds and substantially outperforms MATCHA and DIFT at PCK<sub>@.063</sub> (16px). DIFT leads at the strictest threshold on MSK-Bone.

**Mask propagation.** Using only a single annotated source frame, Match4Annotate matches UniverSeg 5-shot and approaches to 10-shot performance. This substantially outperforms all 1-shot baselines including Matcher and UniverSeg 1-shot on both the EchoNet and MSK-Bone datasets. Unlike segmentation-only approaches, our method also returns point correspondences, enabling unified transfer of points and masks.

## 4.3 Intra-Video Propagation

Tab. 2 reports intra-video results, with qualitative examples provided in the Supplementary Material. While not our primary contribution, Match4-Annotate demonstrates competitive performance against methods specifically designed for temporal tracking.

**Point tracking.** On EchoNet, Match4Annotate underperforms dedicated video tracking models that are explicitly trained for temporal point tracking. On MSK-POI, Match4Annotate surpasses TAPNext but remains below CoTracker3 and TrackOn2. On MSK-Bone, the gap narrows considerably: our  $\delta_{\text{avg}}$  approaches CoTracker3 and outperforms both TAPNext and TrackOn2.

**Mask propagation.** Match4Annotate achieves Dice scores close to SAM 2 on EchoNet while has suboptimal performance on MSK-Bone. We attribute this

**Table 3: Ablation studies** on EchoNet. Feature INR denotes the SIREN-based implicit neural feature representation; Flow Prior denotes the displacement SIREN for flow-guided matching. Best in **bold**, second underlined.

Variant	Feature INR	Flow Prior	Inter-video (200 pairs)		Intra-video (100 videos)	
			PCK <sub>@.016/.031/.063</sub> ↑	Dice ↑	$\delta_{\text{avg}}$ ↑	Dice ↑
Full model	✓	✓	<b>6.1</b> / <b>18.4</b> / <b>46.7</b>	<b>76.3±12.3</b>	<u>31.7±11.5</u>	<b>85.1±6.5</b>
<i>Matching Strategy:</i>						
w/o prior	✓		<u>5.2</u> / <u>16.2</u> / 39.9	71.4±14.4	27.9±9.8	80.7±9.7
prior from source	✓		2.0 / 7.9 / 25.0	63.4±14.8	22.2±11.1	74.8±7.1
<i>Feature Representation:</i>						
Low-Res (28×28)		✓	3.4 / 12.6 / 36.8	72.2±12.0	27.7±9.6	81.3±6.7
Large Image (112×112)		✓	4.6 / 14.9 / <u>40.3</u>	<u>73.9±10.7</u>	<b>33.4±11.8</b>	<u>84.8±6.9</u>

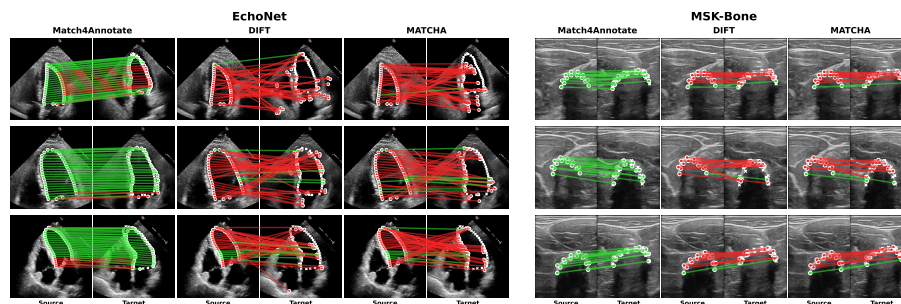


**Fig. 3: Visualization of inter-video point propagation** on EchoNet (left) and MSK-Bone (right). Each cell shows a source frame with annotated points (left) and a target frame with propagated predictions (right). Green lines indicate correct correspondences and red lines indicate incorrect correspondences.

gap to our mask-transfer step, which relies on kernel-density aggregation over matched points and is better suited to larger, smoother regions. In MSK-Bone the target structure is thin and highly non-convex, making it more sensitive to small correspondence errors. Overall, Match4Annotate trades some intra-video performance for a single unified pipeline that propagates both points and masks within and across videos.

#### 4.4 Ablation Studies

Tab. 3 validates our key design choices employing the EchoNet dataset for both inter-video and intra-video propagation.

**Flow prior.** Removing the learned displacement field (“w/o prior”: pure feature matching without spatial prior) consistently degrades both PCK and Dice for inter-video propagation, confirming that the flow-guided spatial prior (Sec. 3.4) substantially improves correspondence accuracy. Using the source position as a fixed prior (“prior from source”: Gaussian centered at the source

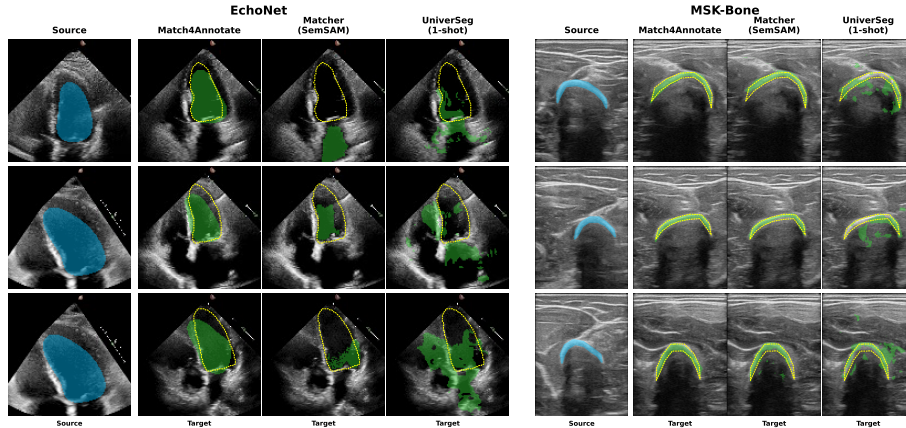


**Fig. 4: Visualization of inter-video mask propagation** on EchoNet (left) and MSK-Bone (right). Each cell shows the target frame with the propagated mask (green) and ground-truth contour (yellow dashed); the leftmost column shows the source reference mask (cyan).

point location, assuming no displacement) performs worst among all variants, demonstrating that the learned displacement field captures meaningful anatomical deformations rather than merely regularizing the search space.

**Implicit neural representation of features vs. direct features.** Replacing the SIREN feature field with direct DINOv3 features reveals a resolution–generalization trade-off. At native resolution (Low-Res,  $28 \times 28$ ), performance drops across all metrics. Increasing the input image size to produce  $112 \times 112$  feature maps (Large Image) yields the best intra-video  $\delta_{avg}$  among all variants, but inter-video performance remains below the full model. This suggests that the continuous SIREN representation provides smoother, more generalizable features for cross-video matching, while direct high-resolution features better preserve fine-grained temporal detail for within-video tracking.

#### 4.5 Qualitative Analysis

We visualize representative challenging inter-video pairs in Figs. 3 and 4, where source and target subjects exhibit anatomical variation to stress-test cross-video transfer. For point propagation (Fig. 3), pairwise matching baselines such as DIFT and MATCHA frequently produce inconsistent correspondences, often swapping left–right symmetric points on both datasets and additionally confusing top–bottom points on EchoNet, resulting in tangled matches and distorted contours. In contrast, Match4Annotate yields mostly ordered, near-parallel correspondences that preserve the overall contour geometry, even when a minority of points fall outside the distance threshold.

For mask propagation (Fig. 4), one-shot segmentation baselines fail in complementary ways. On EchoNet, where neighboring chambers have similar appear-

ance and can be spatially adjacent in the apical view, Matcher and UniverSeg (1-shot) segment the wrong chamber or produce empty/fragmented masks. On MSK-Bone, the thin, curved bone surface offers little tolerance to localization error, and baselines commonly under-segment or produce disconnected regions. Match4Annotate more consistently localizes the target as a single connected region that follows the ground truth, with occasional leakage in difficult cardiac cases.

These differences stem from two design choices. First, the smooth flow prior promotes spatially coherent correspondences, reducing symmetric swaps. Second, the continuous SIREN feature field provides high-resolution, locally consistent features that suppress outlier matches.

## 5 Conclusion

We introduced Match4Annotate, a lightweight framework for intra-video and inter-video propagation of point and mask annotations. Match4Annotate combines (i) a SIREN-based implicit representation that upsamples DINOv3 features into a continuous, high-resolution spatiotemporal feature field, and (ii) an implicit deformation model that provides a smooth spatial prior for correspondence matching. Together, these components enable unified annotation transfer both within a sequence and across different videos. Importantly, the framework is practical to deploy, optimizing per video in minutes on consumer hardware, without large compute requirements (see Supplementary Materials for details).

Across three clinical ultrasound datasets, Match4Annotate achieves strong cross-video propagation performance, improving over dense correspondence baselines across PCK thresholds and outperforming one-shot segmentation methods for mask transfer. For within-video propagation, it is competitive with specialized trackers and segmenters, while additionally supporting cross-video transfer within the same pipeline. Overall, Match4Annotate provides a practical propagation tool that can reduce annotation effort in specialized video domains.

**Limitations.** Our smoothness priors, while effective for medical ultrasound, can struggle with large, rapid displacements common in natural RGB videos (see Supplementary TAP-DAVIS results). The coordinate-only input design may require adaptation for other imaging modalities. Additionally, our method does not explicitly handle occlusions, which may limit performance under significant overlap or self-occlusion.

**Broader Impact.** Match4Annotate addresses annotation scarcity in specialized domains where expert labels are expensive. By enabling annotation propagation, our method can reduce the linear scaling of labeling costs with dataset size, potentially democratizing access to large-scale video analysis in medical imaging and other high-expertise domains.

## References

1. Aydemir, G., Cai, X., Xie, W., Güney, F.: Track-On: Transformer-based online point tracking with memory. In: The Thirteenth International Conference on Learning Representations (2025)
2. Aydemir, G., Xie, W., Güney, F.: Track-On2: Enhancing online point tracking with memory. arXiv preprint arXiv:2509.19115 (2025)
3. Butoi\*, V.I., Ortiz\*, J.J.G., Ma, T., Sabuncu, M.R., Guttag, J., Dalca, A.V.: Universeg: Universal medical image segmentation. International Conference on Computer Vision (2023)
4. Caron, M., Touvron, H., Misra, I., Jégou, H., Mairal, J., Bojanowski, P., Joulin, A.: Emerging properties in self-supervised vision transformers. In: ICCV (2021)
5. Cheng, H.K., Chen, S., Tsai, Y.H., Lin, Y.C., Yang, M.H.: Rethinking space-time networks with improved memory coverage for efficient video object segmentation. In: Advances in Neural Information Processing Systems (NeurIPS) (2021)
6. Cheng, H.K., Schwing, A.G.: Xmem: Long-term video object segmentation with an atkinson-shiffrin memory model. In: ECCV (2022)
7. DeTone, D., Malisiewicz, T., Rabinovich, A.: Superpoint: Self-supervised interest point detection and description. In: Proceedings of the IEEE Conference on Computer Vision and Pattern Recognition (CVPR) Workshops. pp. 224–236 (June 2018)
8. Doersch, C., Gupta, A., Markeeva, L., Recasens, A., Smaira, L., Aytar, Y., Carreira, J., Zisserman, A., Yang, Y.: TAP-vid: A benchmark for tracking any point in a video. Advances in Neural Information Processing Systems **35**, 13610–13626 (2022)
9. Doersch, C., Gupta, A., Markeeva, L., Recasens, A., Smaira, L., Aytar, Y., Carreira, J., Zisserman, A., Yang, Y.: TAP-Vid: A benchmark for tracking any point in a video. In: Advances in Neural Information Processing Systems (NeurIPS) (2022)
10. Dosovitskiy, A., Beyer, L., Kolesnikov, A., Weissenborn, D., Zhai, X., Unterthiner, T., Dehghani, M., Minderer, M., Heigold, G., Gelly, S., Uszkoreit, J., Houlsby, N.: An image is worth 16x16 words: Transformers for image recognition at scale. In: International Conference on Learning Representations (ICLR) (2021)
11. Edstedt, J., Sun, Q., Bökman, G., Wadenbäck, M., Felsberg, M.: Roma: Robust dense feature matching. In: CVPR (2024)
12. Fu, S., Hamilton, M., Brandt, L., Feldmann, A., Zhang, Z., Freeman, W.T.: Featup: A model-agnostic framework for features at any resolution. In: International Conference on Learning Representations (ICLR) (2024), <https://openreview.net/forum?id=GkJiNn2QDF>
13. Karaev, N., Makarov, Y., Wang, J., Neverova, N., Vedaldi, A., Rupprecht, C.: Cotracker3: Simpler and better point tracking by pseudo-labelling real videos. In: Proceedings of the IEEE/CVF International Conference on Computer Vision (ICCV). pp. 6013–6022 (October 2025)
14. Karaev, N., Rocco, I., Graham, B., Neverova, N., Vedaldi, A., Rupprecht, C.: Cotracker: It is better to track together. In: European Conference on Computer Vision (2024)
15. Kingma, D.P., Ba, J.: Adam: A method for stochastic optimization. In: International Conference on Learning Representations (ICLR) (2015)
16. Kirillov, A., Mintun, E., Ravi, N., Mao, H., Rolland, C., Gustafson, L., Xiao, T., Whitehead, S., Berg, A.C., Lo, W.Y., Dollár, P., Girshick, R.: Segment anything. In: Proceedings of the IEEE/CVF International Conference on Computer Vision (ICCV). pp. 4015–4034 (2023)

17. Li, F., Zhang, H., Sun, P., Zou, X., Liu, S., Yang, J., Li, C., Zhang, L., Gao, J.: Segment and recognize anything at any granularity. In: European Conference on Computer Vision (ECCV) (2024)
18. Lindenberger, P., Sarlin, P.E., Pollefeys, M.: Lightglue: Local feature matching at light speed. In: Proceedings of the IEEE/CVF International Conference on Computer Vision (ICCV). pp. 17627–17638 (October 2023)
19. Liu, Y., Zhu, M., Li, H., Chen, H., Wang, X., Shen, C.: Matcher: Segment anything with one shot using all-purpose feature matching. In: International Conference on Learning Representations (ICLR) (2024), [https://proceedings.iclr.cc/paper\\_files/paper/2024/hash/4df9a5e6bad9e64ebcea453e031142bb-Abstract-Conference.html](https://proceedings.iclr.cc/paper_files/paper/2024/hash/4df9a5e6bad9e64ebcea453e031142bb-Abstract-Conference.html)
20. Mildenhall, B., Srinivasan, P.P., Tancik, M., Barron, J.T., Ramamoorthi, R., Ng, R.: Nerf: Representing scenes as neural radiance fields for view synthesis. In: ECCV (2020)
21. Müller, T., Evans, A., Schied, C., Keller, A.: Instant neural graphics primitives with a multiresolution hash encoding. In: ACM transactions on graphics. vol. 41, pp. 1–15 (2022)
22. Oquab, M., Darcet, T., Moutakanni, T., Vo, H., Szafraniec, M., Khalidov, V., Fernandez, P., Haziza, D., Massa, F., El-Nouby, A., et al.: Dinov2: Learning robust visual features without supervision. In: Proceedings of the International Conference on Machine Learning (2023)
23. Ouyang, D., He, B., Ghorbani, A., Yuan, N., Ebinger, J., Langlotz, C.P., Heidenreich, P.A., Harrington, R.A., Liang, D.H., Ashley, E.A., et al.: Video-based ai for beat-to-beat assessment of cardiac function. *Nature* **580**(7802), 252–256 (2020)
24. Pallarès-López, R., Folgado, D., Magana-Salgado, U., Rosendorf, J., Ryu, E., Feigin-Almon, M., Gamboa, H., Daniel, L., Anthony, B.W., Namburi, P.: A multi-modal biomechanics dataset with synchronized kinematics and internal tissue motions during reaching (2026). <https://doi.org/10.6084/m9.figshare.31030252>
25. Potje, G., Cadar, F., Araujo, A., Martins, R., Nascimento, E.R.: Xfeat: Accelerated features for lightweight image matching. In: Proceedings of the IEEE/CVF Conference on Computer Vision and Pattern Recognition (CVPR). pp. 2682–2691 (June 2024)
26. Ravi, N., Gabeur, V., Hu, Y.T., Hu, R., Ryali, C., Ma, T., Khedr, H., Rädle, R., Rolland, C., Gustafson, L., et al.: SAM 2: Segment anything in images and videos. In: Advances in Neural Information Processing Systems (NeurIPS). vol. 37 (2024)
27. Rombach, R., Blattmann, A., Lorenz, D., Esser, P., Ommer, B.: High-resolution image synthesis with latent diffusion models. In: Proceedings of the IEEE/CVF Conference on Computer Vision and Pattern Recognition (CVPR) (2022)
28. Siméoni, O., Vo, H.V., Seitzer, M., Baldassarre, F., Oquab, M., Jose, C., Khalidov, V., Szafraniec, M., Yi, S., Ramamonjisoa, M., Massa, F., Haziza, D., Wehrstedt, L., Wang, J., Darcet, T., Moutakanni, T., Sentana, L., Roberts, C., Vedaldi, A., Tolan, J., Brandt, J., Couprie, C., Mairal, J., Jégou, H., Labatut, P., Bojanowski, P.: Dinov3 (2025). <https://doi.org/10.48550/arXiv.2508.10104>
29. Sitzmann, V., Martel, J.N., Bergman, A.W., Lindell, D.B., Wetzstein, G.: Implicit neural representations with periodic activation functions. In: Advances in Neural Information Processing Systems (NeurIPS) (2020)
30. Sun, Y., Wang, X., Liu, Z., Miller, J., Efros, A., Hardt, M.: Test-time training with self-supervision for generalization under distribution shifts. In: ICML (2020)
31. Tancik, M., Srinivasan, P.P., Mildenhall, B., Fridovich-Keil, S., Raghavan, N., Singhal, U., Ramamoorthi, R., Barron, J.T., Ng, R.: Fourier features let networks learn

- high frequency functions in low dimensional domains. In: *Advances in Neural Information Processing Systems (NeurIPS)* (2020)
32. Tang, L., Jia, M., Wang, Q., Phoo, C.P., Hariharan, B.: Emergent correspondence from image diffusion. In: *NeurIPS* (2023)
  33. Teed, Z., Deng, J.: Raft: Recurrent all-pairs field transforms for optical flow. In: *ECCV* (2020)
  34. Tyszkiewicz, M.J., Fua, P., Trulls, E.: DISK: Learning local features with policy gradient. In: *Advances in Neural Information Processing Systems (NeurIPS)*. vol. 33, pp. 14254–14265 (2020)
  35. UC Davis Department of Radiology: Research rates (2024), uC Davis Health, Department of Radiology research service rates. Radiologist professional time: \$334/hour (internal/federally funded), \$454/hour (external non-profit), \$613/hour (external for-profit)
  36. Wang, D., Shelhamer, E., Liu, S., Olshausen, B., Darrell, T.: Tent: Fully test-time adaptation by entropy minimization. In: *International Conference on Learning Representations* (2021)
  37. Wang, Y., Yao, Q., Kwok, J.T., Ni, L.M.: Generalizing from a few examples: A survey on few-shot learning. In: *ACM computing surveys*. vol. 53, pp. 1–34 (2020)
  38. Xie, Y., Takikawa, T., Saito, S., Litany, O., Yan, S., Khan, N., Tombari, F., Tompkin, J., Sitzmann, V., Sridhar, S.: Neural fields in visual computing and beyond (2021). <https://doi.org/10.48550/arXiv.2111.11426>
  39. Xu, H., Zhang, J., Cai, J., Rezatofighi, H., Tao, D.: Gmflow: Learning optical flow via global matching. In: *CVPR* (2022)
  40. Xue, F., Elflein, S., Leal-Taixé, L., Zhou, Q.: MATCHA: Towards matching anything. *arXiv preprint arXiv:2501.14945* (2025)
  41. Zholus, A., Doersch, C., Yang, Y., Koppula, S., Patraucean, V., He, X.O., Rocco, I., Sajjadi, M.S.M., Chandar, S., Goroshin, R.: Tapnext: Tracking any point (tap) as next token prediction. In: *ICCV* (2025)

## Supplementary Materials

### A Justification of SIREN over Alternative INR Architectures

We choose SIREN [29] over three alternative implicit neural representations: (1) ReLU MLP, (2) ReLU MLP with sinusoidal positional encoding (ReLU+PE) [20], and (3) Instant-NGP with multi-resolution hash encoding [21]. Below we provide quantitative evidence for the choice.

We compare the four architectures on 5 randomly selected EchoNet videos using identical training budgets (500 epochs). For ReLU+PE, we use  $L=3$  positional encoding frequencies based on our ablation study, which showed that higher values introduce crosshatch artifacts. All models use 2 hidden layers with 256 hidden dimensions; Instant-NGP additionally uses a 16-level multi-resolution hash grid.

**Table A1: Architecture comparison.** Reconstruction quality (mean  $\pm$  std over 5 videos). Best in **bold**.

Architecture	Params	Recon. Loss $\downarrow$	RMSE $\downarrow$
<b>SIREN (ours)</b>	165,520	<b>0.0038</b> $\pm$ 0.0004	<b>0.0613</b>
ReLU MLP	165,520	0.0237 $\pm$ 0.0026	0.1540
ReLU+PE ( $L=3$ )	170,128	0.0122 $\pm$ 0.0019	0.1103
Instant-NGP	16,950,160	0.0253 $\pm$ 0.0058	0.1591

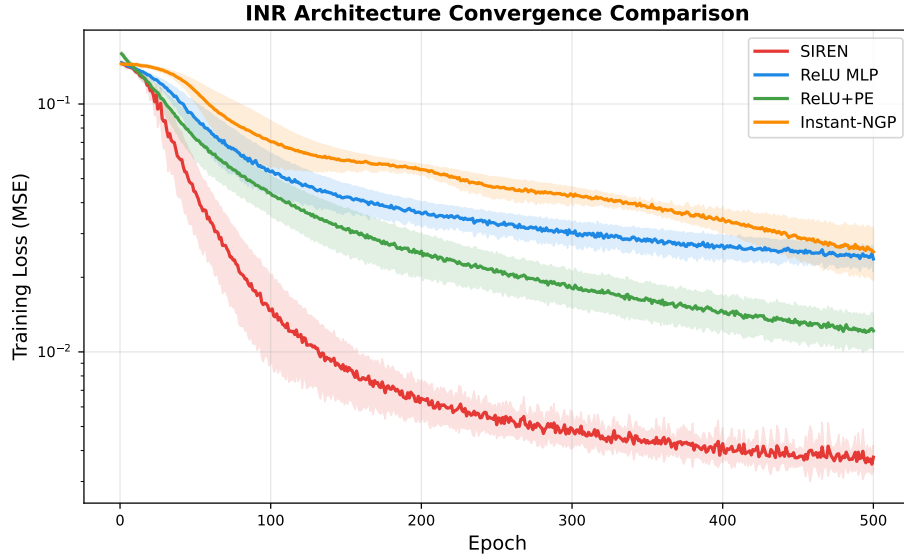
SIREN achieves  $3\times$  lower reconstruction loss than the next best alternative (ReLU+PE), with  $100\times$  fewer parameters than Instant-NGP. ReLU+PE with reduced positional encoding frequencies ( $L=3$ ) significantly improves over the default  $L=10$  setting by mitigating crosshatch artifacts, but still lags behind SIREN. Instant-NGP, despite its large parameter count ( $\sim 17$ M), fails to learn smooth feature fields suitable for continuous coordinate queries.

Fig. A1 shows training convergence curves (loss vs. epoch) for all four architectures, averaged over 5 videos. SIREN converges to a substantially lower loss within the first 100 epochs.

Fig. A2 shows PCA-projected feature maps for all four architectures alongside the low-resolution DINOv3 features. SIREN produces visually smooth, high-fidelity feature maps, while ReLU-based networks exhibit blocky artifacts and Instant-NGP shows noisy, fragmented features.

### B Network Architecture and Training Details

Match4Annotate uses three neural networks: (1) a feature field SIREN  $f_\theta$  that maps spatiotemporal coordinates to dense feature vectors, (2) a learned convolutional downsampler  $\mathcal{D}$  used during training to bridge the resolution gap



**Fig. A1: Training convergence.** Reconstruction loss vs. epoch for four INR architectures (mean  $\pm$  std over 5 EchoNet videos). SIREN converges the fastest and to the lowest loss.

**Table A2: Architecture configurations** used in the comparison experiment.

Architecture	Hidden Layers	$\omega_0$	Frequencies	Hash levels	Params
SIREN	256	2	30.0	–	165,520
ReLU MLP	256	2	–	–	165,520
ReLU+PE	256	2	–	3	170,128
Instant-NGP	256	2	–	–	16,950,160

between the implicit neural representation output and the VFM supervision, and (3) a displacement SIREN  $g_\phi$  that predicts per-pixel spatial deformations for flow-guided matching.

### B.1 Feature Field SIREN ( $f_\theta$ )

**Architecture.**  $f_\theta : \mathbb{R}^3 \rightarrow \mathbb{R}^D$  is a SIREN network with periodic activation  $\phi(x) = \sin(\omega_0 x)$ . The network consists of  $L$  fully-connected hidden layers, each of dimension  $H_{\text{dim}}$ , with a final linear projection to the feature dimension  $D$ . For an input coordinate  $\mathbf{c} = (x, y, t) \in [-1, 1]^3$ :

$$\mathbf{h}_0 = \sin(\omega_0(\mathbf{W}_0 \mathbf{c} + \mathbf{b}_0)) \quad (\text{B1})$$

$$\mathbf{h}_l = \sin(\omega_0(\mathbf{W}_l \mathbf{h}_{l-1} + \mathbf{b}_l)), \quad l = 1, \dots, L-1 \quad (\text{B2})$$

$$f_\theta(\mathbf{c}) = \mathbf{W}_L \mathbf{h}_{L-1} + \mathbf{b}_L \quad (\text{B3})$$

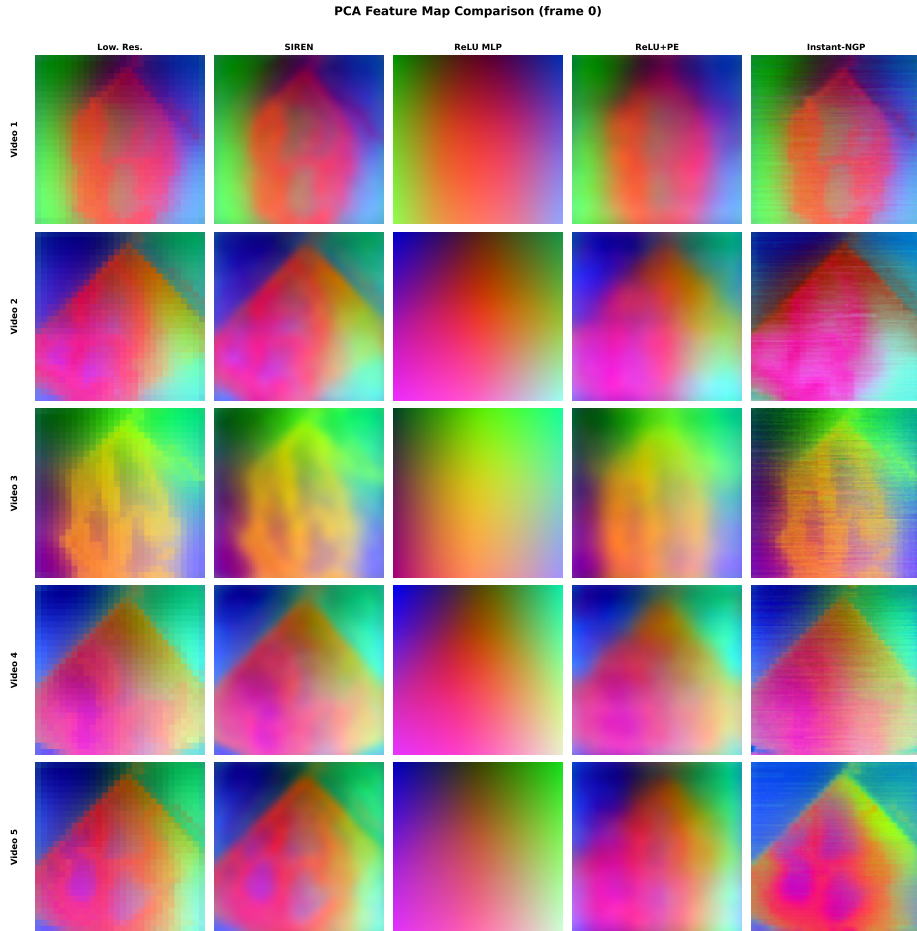


**Fig. A2: PCA feature maps.** RGB visualization of the first three PCA components of the reconstructed feature field for the first frame of five EchoNet videos. Left column: low-resolution DINOv3 features. SIREN produces the most faithful reconstruction, while alternatives show blocky artifacts (ReLU MLP, ReLU+PE) or fragmented features (Instant-NGP).

**Weight initialization.** Following Sitzmann *et al.* [29], the first layer weights are initialized as  $W_0 \sim \mathcal{U}(-1/d_{\text{in}}, +1/d_{\text{in}})$  where  $d_{\text{in}} = 3$  is the input dimension. Subsequent layer weights are initialized as  $W_l \sim \mathcal{U}(-\sqrt{6/n}/\omega_0, +\sqrt{6/n}/\omega_0)$  where  $n$  is the layer fan-in. All biases are initialized to zero.

**Training.** We train  $f_\theta$  jointly with the downsampler  $\mathcal{D}$  to reproduce frozen VFM features at high resolution using the reconstruction loss (Eq. 3 in the main

paper):

$$\mathcal{L}_{\text{recon}} = \frac{1}{N} \sum_{i=1}^N \|\mathcal{D}(f_{\theta}(x_i, y_i, t_i)) - F_{t_i}(x_i, y_i)\|_2^2 \quad (\text{B4})$$

where  $F_t \in \mathbb{R}^{H' \times W' \times D}$  are DINOv3-ViT-S/16 features.

**Table B3: Feature field SIREN hyperparameters.**

Parameter	Value
Hidden dimension ( $H_{\text{dim}}$ )	256
Number of hidden layers ( $L$ )	2
Output dimension ( $D$ )	384
Activation frequency ( $\omega_0$ )	30.0
Output resolution ( $H \times W$ )	112 × 112 for echonet, 224 × 224 for MSK
Training epochs	500
Batch size	1024 coordinates
Optimizer	Adam ( $\beta_1=0.9, \beta_2=0.999$ )
Learning rate	$10^{-4}$

## B.2 Convolutional Downsampler ( $\mathcal{D}$ )

The feature field SIREN outputs features on a high-resolution grid  $\Omega_{\text{HR}}$  of size  $H \times W$ , while VFM supervision is available at the native patch-token resolution  $H' \times W'$ . The downsampler  $\mathcal{D} : \mathbb{R}^{H \times W \times D} \rightarrow \mathbb{R}^{H' \times W' \times D}$  bridges this resolution gap during training.

**Architecture.** We followed [12] and used a learned depthwise convolution. A single learnable kernel  $\mathbf{K} \in \mathbb{R}^{k_H \times k_W}$  is shared across all  $D$  feature channels (depthwise convolution). To ensure the downsampler acts as a proper weighted average:

1. **Non-negativity:** Kernel weights are passed through  $|\cdot|$  (absolute value).
2. **Normalization:** Weights are divided by their sum:  $\tilde{K}_{ij} = |K_{ij}| / \sum_{i,j} |K_{ij}|$ .

This guarantees that the downsampled features remain in the same value range as the high-resolution output, preventing training instability. The kernel size is automatically determined from the input/target resolution ratio: stride =  $H/H'$ , kernel size = stride +  $\mathbb{1}[H \bmod H' > 0]$ . For our default configuration (224→28), this yields stride = 8 and kernel size  $8 \times 8$ .

## B.3 Displacement SIREN ( $g_{\phi}$ )

**Architecture.** The displacement SIREN  $g_{\phi} : \mathbb{R}^2 \rightarrow \mathbb{R}^2$  predicts per-coordinate spatial displacements  $(\Delta x, \Delta y) = g_{\phi}(x, y)$ . We use a single-hidden-layer (“wide”) SIREN, acting as a learned Fourier basis expansion. A separate displacement SIREN is trained for each source–target frame pair.

**Training loss.** The displacement field is optimized to align features between source and target frames (Eq. 5 in the main paper):

$$\mathcal{L}_{\text{flow}} = \frac{1}{M} \sum_{i=1}^M \|f_{\theta}(x_i + \Delta x_i, y_i + \Delta y_i, t_{\text{tgt}}) - f_{\theta}(x_i, y_i, t_{\text{src}})\|_2^2 + \lambda_1 \cdot \mathcal{L}_{\text{TV}} + \lambda_2 \cdot \mathcal{L}_{\text{L1}} \quad (\text{B5})$$

where  $\mathcal{L}_{\text{TV}}$  encourages spatial smoothness of the displacement field, and  $\mathcal{L}_{\text{L1}} = \frac{1}{M} \sum_i \|g_{\phi}(x_i, y_i)\|_1$  penalizes overall displacement magnitudes, acting as a prior avoiding unnecessary deformation on flat regions.

**Inference.** Given a source annotation point  $\mathbf{p}^s$ , we predict the displacement  $g_{\phi}(\mathbf{p}^s) = (\Delta x, \Delta y)$  and compute the flow-predicted center  $\tilde{\mathbf{p}} = \mathbf{p}^s + g_{\phi}(\mathbf{p}^s)$ . This predicted location serves as the center of a Gaussian spatial prior for flow-guided matching (Eq. 7 in the main paper).

**Table B4: Displacement SIREN hyperparameters.**

Parameter	Value
Input dimension	2
Hidden dimension	128
Number of hidden layers	1
Output dimension	2
$\omega_0$	30.0
Training epochs	1000
Optimizer	Adam
Learning rate	$10^{-4}$
$\lambda_1$ (TV)	10.0
$\lambda_2$ (L1)	0.01

## C Mask Reconstruction via Interior Point KDE

### C.1 Interior Point Extraction

Given a source binary mask  $M_{\text{src}}$ , we extract a dense set of interior points using the Euclidean distance transform (EDT). For each pixel  $(x, y)$  within the mask, we compute its distance to the nearest background pixel:

$$\text{EDT}(x, y; M_{\text{src}}) = \min_{(x', y') \notin M_{\text{src}}} \sqrt{(x - x')^2 + (y - y')^2} \quad (\text{C6})$$

We select interior points as those with sufficient distance from the boundary:

$$\mathcal{I}_{\text{src}} = \{(x, y) \mid \text{EDT}(x, y; M_{\text{src}}) \geq d_{\text{min}}\} \quad (\text{C7})$$

where  $d_{\min} = 2$  pixels. This excludes ambiguous boundary pixels while densely covering the annotated region. The resulting point set typically contains hundreds to thousands of points, depending on mask size.

## C.2 Point Propagation

All interior points  $\mathbf{p} \in \mathcal{I}_{\text{src}}$  are independently propagated to the target frame using the flow-guided matching strategy (Sec. 3.4 in the main paper). Each point  $\mathbf{p}$  is mapped to its corresponding location  $\mathbf{p}^*$  in the target frame, producing a propagated interior point set  $\mathcal{I}_{\text{tgt}}$ .

## C.3 Probability Field via KDE

The propagated points are converted to a continuous probability map using kernel density estimation with a Gaussian kernel:

$$P(x, y) = \frac{1}{Z} \sum_{\mathbf{p}_k^* \in \mathcal{I}_{\text{tgt}}} \exp\left(-\frac{(x - x_k^*)^2 + (y - y_k^*)^2}{2\sigma_{\text{KDE}}^2}\right) \quad (\text{C8})$$

where  $Z$  normalizes  $P$  to  $[0, 1]$ , and  $\sigma_{\text{KDE}}$  controls the Gaussian bandwidth (smoothness of the probability field).

**Implementation.** We first create a discrete hit map on the annotation canvas by accumulating 1.0 at each propagated point’s integer pixel coordinate. We then convolve this hit map with a 2D Gaussian filter and normalize by dividing by the maximum value.

## C.4 Binary Mask via Thresholding

The predicted binary mask is obtained by thresholding the probability field:

$$M_{\text{pred}}(x, y) = \mathbf{1}[P(x, y) \geq \tau] \quad (\text{C9})$$

where  $\tau$  is the probability threshold.

## C.5 KDE Parameter Sensitivity

The KDE reconstruction introduces two tunable parameters: the Gaussian bandwidth  $\sigma_{\text{KDE}}$  and the threshold  $\tau$ . In our annotation tool, these parameters are exposed to users to allow flexible control over the reconstructed mask depending on the desired level of spatial smoothing and tolerance to point noise. Intuitively,  $\sigma_{\text{KDE}}$  controls the spatial spread of each propagated interior point, while  $\tau$  determines the decision boundary for converting the continuous probability field into a binary mask. These parameters influence the morphology of the reconstructed segmentation:

**Small  $\sigma_{\text{KDE}}$  or high  $\tau$ :** produces conservative masks but may lead to fragmented or disconnected regions if propagated points are sparse or slightly misaligned.

**Large  $\sigma_{\text{KDE}}$  or low  $\tau$ :** produces smoother and more connected masks but may over-expand the segmentation, covering adjacent regions beyond the structure of interest.

For the experimental results reported in the main paper, we determine fixed parameter values using a small validation set with 10 videos on both EchoNet-Dynamic and MSK-Bone. For EchoNet-Dynamic, we used  $\sigma_{\text{KDE}} = 6.0$ ,  $\tau = 0.25$ , while for MSK-Bone, we used  $\sigma_{\text{KDE}} = 2.0$ ,  $\tau = 0.01$ .

## D Additional Inter-Video Propagation Examples

We provide additional qualitative examples of inter-video annotation propagation across two datasets (EchoNet and MSK-Masks), extending Figs. 3 and 4 in the main paper, and showing intermediate frames in the videos beyond those with ground truth annotations.

### D.1 Inter-Video Point Propagation

Fig. D3 shows 6 inter-video pairs: 3 EchoNet cardiac ultrasound pairs and 3 MSK-Bone musculoskeletal pairs. For each pair, the source frame (left) shows annotated contour points, and the target frame (right) shows predicted points (colored circles) alongside ground-truth locations (white crosses, if available). Across both datasets and anatomical domains, Match4Annotate produces anatomically coherent point correspondences.

### D.2 Inter-Video Mask Propagation

Fig. D4 shows mask propagation for the same 6 pairs. The source mask (blue fill) is propagated to the target video via interior-point matching and KDE reconstruction. Predicted masks (green fill) are overlaid with ground-truth contours (yellow dashed, if available). Match4Annotate produces masks that closely follow the ground-truth shape across both the small-canvas EchoNet ( $112 \times 112$ ) and high-resolution MSK-Masks ( $656 \times 496$ ) domains.

## E Intra-Video Propagation Examples

We present qualitative examples of intra-video annotation propagation across all three datasets, demonstrating Match4Annotate’s ability to transfer annotations from a single labeled frame to intermediate frames spanning the entire video timeline.

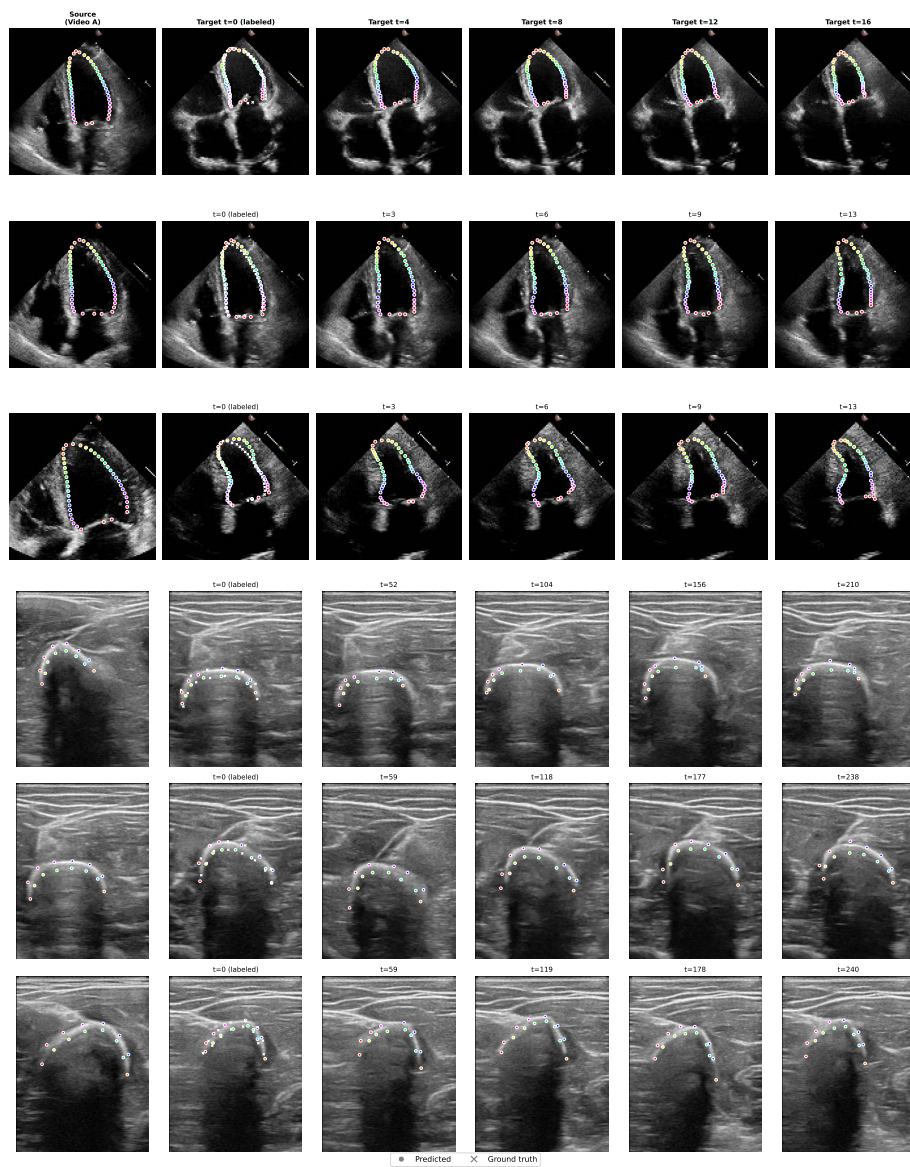


**Fig. D3: Inter-video point propagation** on EchoNet (top 3 rows) and MSK-Masks (bottom 3 rows). Each row: source frame with annotated points (left) and target prediction with GT overlay (right). Colored circles = predicted, white crosses = ground truth.

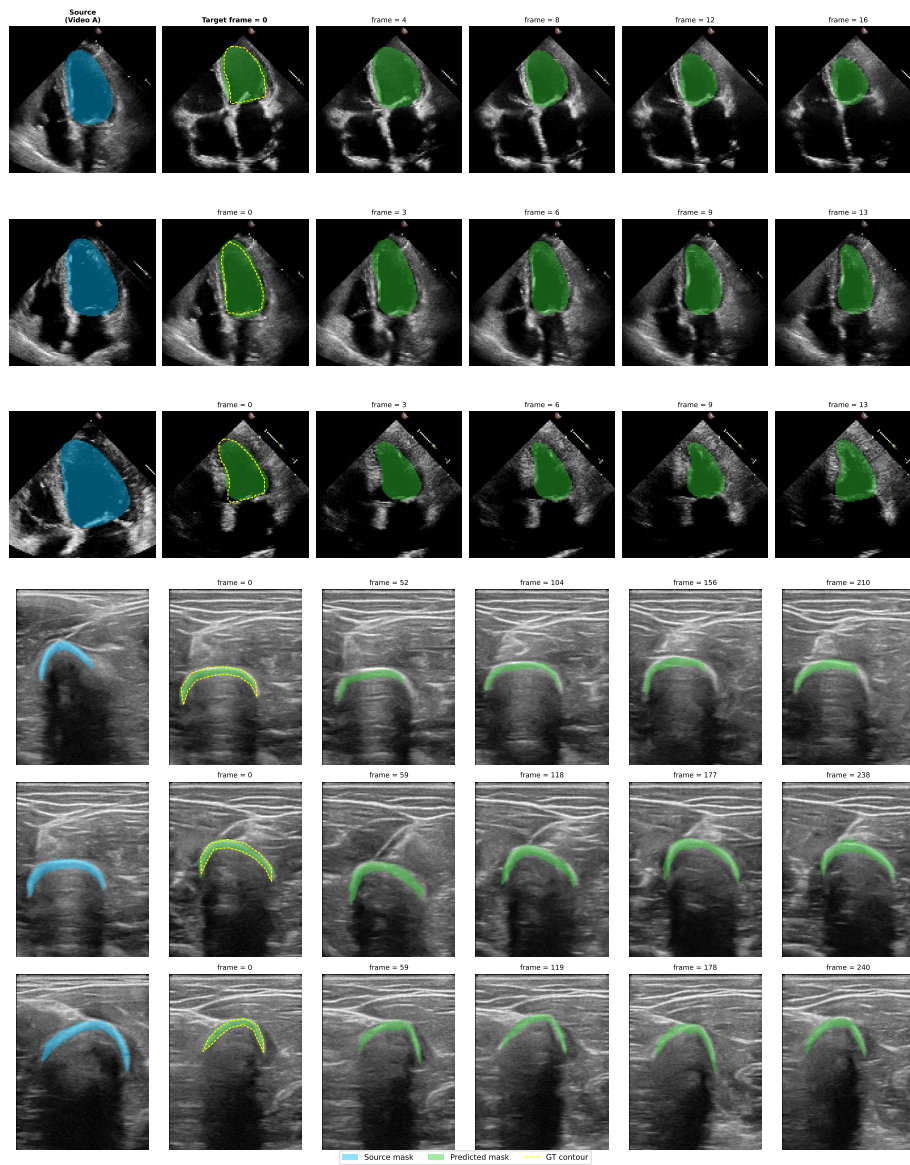


**Fig. D4: Inter-video mask propagation** on EchoNet (top 3 rows) and MSK-Masks (bottom 3 rows). Same pairs as Fig. D3. Blue fill = source mask, green fill = predicted mask, yellow dashed = GT contour.

### E.1 Intra-Video Point Tracking

Fig. E5 shows temporal progression strips for intra-video point propagation on MSK-Points (musculoskeletal reaching motion). Each strip shows the source

frame with ground-truth annotations followed by 7 evenly-spaced target frames across the video, including intermediate non-labeled frames. Predicted point locations (colored circles) track anatomical landmarks accurately through the reaching motion cycle, demonstrating smooth temporal propagation.

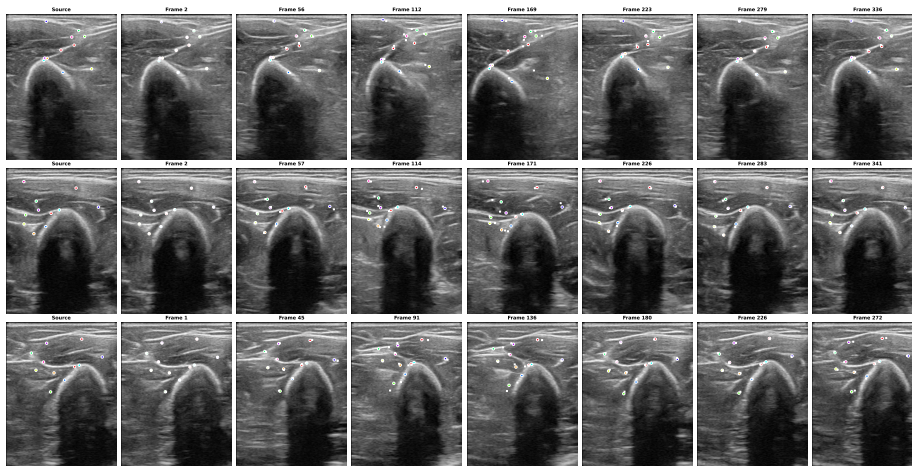


**Fig. E5: Intra-video point tracking** on MSK-Points. Two videos shown as temporal strips. Left: source frame with GT annotations. Right: 7 target frames at evenly-spaced time points across the full video. Colored circles = predicted points, white crosses = ground truth.

## E.2 Intra-Video Mask Propagation

Fig. E6 shows mask propagation temporal strips for EchoNet and MSK-Masks. The source mask (blue fill) is propagated via interior-point matching and KDE reconstruction. Predicted masks (green fill) are shown with ground-truth contours (yellow dashed, if available) at each target frame.

## F Natural Video Evaluation: TAP-DAVIS

To characterize Match4Annotate’s domain scope, we evaluate on TAP-DAVIS [9], a natural video point-tracking benchmark with 30 videos featuring diverse motion patterns and frequent occlusions. Unlike medical ultrasound, natural videos exhibit large inter-frame displacements, complex motion patterns, and object disappearances, all of which challenge our smoothness-based inductive biases.

### F.1 Experimental Setup

We select three videos spanning a difficulty spectrum:

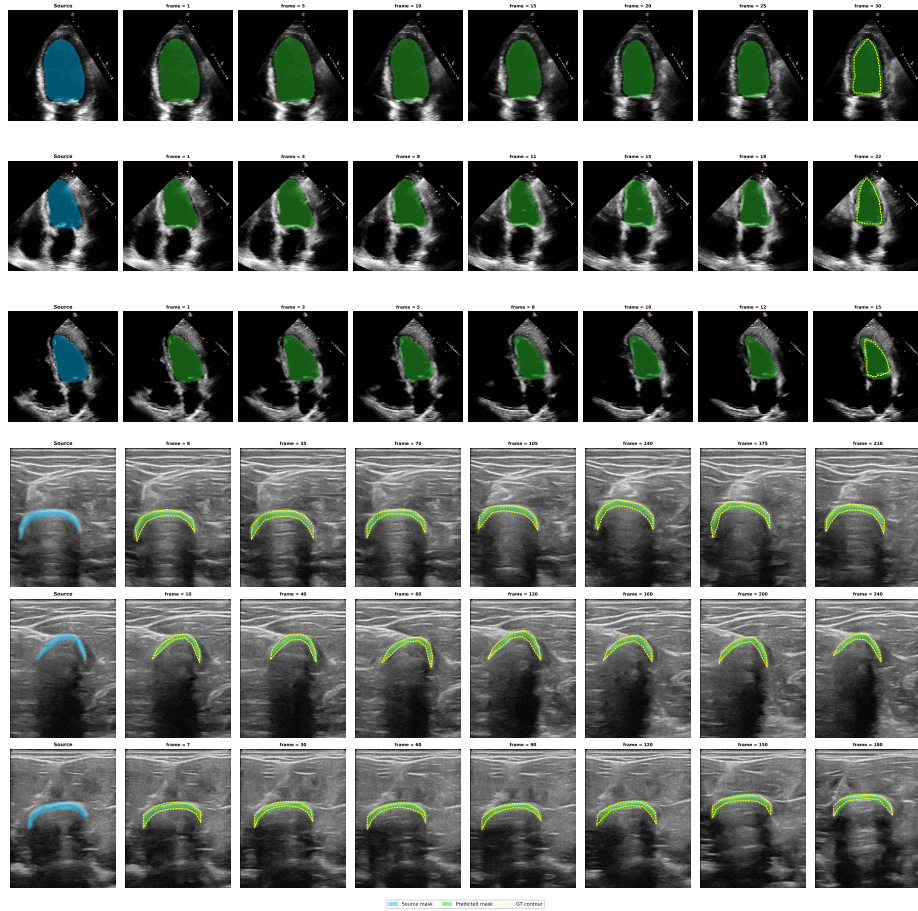


**Fig. E6: Intra-video mask propagation** on EchoNet (top row) and MSK-Masks (bottom two rows). Left: source frame with GT mask. Right: predicted masks (green) with GT contour (yellow dashed) at target frames across the video timeline. Per-frame Dice values shown in titles.

1. **blackswan** (50 frames, 5 points, 0% occlusion): smooth gliding motion, minimal deformation.
2. **camel** (90 frames, 10 points, 16% occlusion): moderate motion with some self-occlusion.
3. **breakdance** (84 frames, 25 points, 35% occlusion): fast articulated motion with frequent occlusions.

We run the full Match4Annotate pipeline. All hyperparameters are identical to those used for MSK-POI (Tables B3 and B4). We report the TAP-Vid  $\delta_{avg}$  metric.

## F.2 Qualitative Results

Fig. F7 shows point tracking strips for each video. For *blackswan*, predicted points closely follow the ground truth across all 50 frames. For *camel*, tracking remains reasonable for visible points but degrades when points become occluded. For *breakdance*, rapid limb motion causes significant tracking drift, particularly for extremities.



**Fig. F7: TAP-DAVIS point tracking.** Each row: source frame (left) and 7 evenly-spaced target frames. Colored circles = predicted, white  $\times$  = visible GT.

## F.3 Tracking Accuracy and Summary

Tab. F5 reports mean  $\delta_{\text{avg}}$  over all target frames for each video. *Blackswan* achieves  $\delta_{\text{avg}} = 0.664$ , consistent with smooth, occlusion-free motion. *Breakdance* drops to  $\delta_{\text{avg}} = 0.333$  when including occluded points, with the gap between visible-only and all-points metrics quantifying the impact of missing occlusion handling.

**Table F5: TAP-DAVIS summary.** Mean  $\delta_{\text{avg}}$  over all target frames.

Video	Points	Occ. %	$\delta_{\text{avg}}$ (vis.)	$\delta_{\text{avg}}$ (all)
blackswan	5	0%	0.664	0.664
camel	6	16%	0.303	0.291
breakdance	21	35%	0.472	0.333

## F.4 Discussion

These results confirm that Match4Annotate excels at smooth-motion domains like cardiac, and musculoskeletal imaging. Three factors limit natural-video performance:

1. **Smoothness priors:** The displacement SIREN assumes smooth spatial deformations, which breaks down for large inter-frame displacements (*e.g.*, limbs traversing half the frame in a few frames).
2. **No occlusion model:** Our method always predicts a location for every source point, with no mechanism to detect or handle disappearances.
3. **Frame-0 propagation:** We propagate from a single source frame, causing errors to compound over time. Dedicated trackers (*e.g.*, CoTracker3 [13], TAPNext [41]) use temporal chaining and recurrent features to mitigate drift.

For natural video with large displacements and occlusions, dedicated video trackers remain more appropriate. Match4Annotate’s value lies in domains where its smoothness inductive bias matches the underlying motion dynamics.

## G Time and Memory Analysis

We report wall-clock timing and peak GPU memory usage for the full Match4Annotate pipeline on a single NVIDIA RTX 4090 (24 GB VRAM) with 32 GB system RAM. All measurements are averaged over 3 repetitions with GPU warmup. The benchmark uses EchoNet (112×112 annotation space) with DINOv3-ViT-S/16 features at 448px input, running the complete pipeline: feature extraction → feature SIREN training → flow SIREN training → flow-guided matching → segmentation mask conversion.

**Table G6: Per-component timing and memory** on NVIDIA RTX 4090. The full pipeline uses 112×112 HR output resolution (matching annotation space) and a single flow SIREN trained once per frame pair.

Component	Time	Std	VRAM (GB)
DINOv3 feature extraction (16 frames, 448px)	63 ms	±2 ms	0.23
Feature SIREN training (500 epochs)	29.2 s	±1.2 s	3.03
Flow SIREN training (1000 epochs, 1 pair)	0.8 s	±0.01 s	0.17
POI inference (42 edge pts)	17 ms	±0 ms	<0.1
Mask inference (500 interior pts)	158 ms	±4 ms	<0.1
KDE mask pipeline (500 pts)	155 ms	±1 ms	<0.1

The feature SIREN training dominates the per-video cost ( $\sim 30$  s). Crucially, each flow SIREN is trained *once* per source–target frame pair and shared across all annotation points, i.e., the 0.8 s flow training cost is amortized whether propagating 42 contour points or 500 interior points for KDE mask reconstruction.

### G.1 GPU Memory Usage

The feature SIREN training with 112×112 output is the most memory-intensive component at  $\sim 3$  GB, well within the capacity of mid-range GPUs. All other

components require negligible VRAM ( $<0.25$  GB). The total pipeline peak of  $\sim 3$  GB makes Match4Annotate deployable on consumer hardware without specialized GPU requirements.

## G.2 Batched Flow Acceleration

For batch evaluation scenarios, we implement GPU-parallel flow SIREN training using `torch.func.vmap` (batched functional API). This trains  $N$  independent 2D flow SIRENs simultaneously by vectorizing over the batch dimension, sharing the same forward/backward pass kernel. Measured speedup on RTX 4090:  $\sim 14\times$  GPU speedup vs. sequential training.

## G.3 Discussion

Match4Annotate requires test-time optimization (training SIRENs per video), which incurs a one-time cost of  $\sim 30$  s per video. This is slower than feed-forward methods (*e.g.*, CoTracker3, SAM 2) which run in seconds. However, once the feature SIREN is trained, propagation to additional target frames costs only  $\sim 0.8$  s each (dominated by flow SIREN training), and adding more annotation points to the same frame pair is essentially free (17 ms for 42 points). This amortized cost structure makes Match4Annotate practical for the annotation propagation use case, where a user annotates one frame and propagates to many others within the same video or across videos sharing a trained feature field.